Resonant self-trapping of high intensity Bessel beams in underdense plasmas

J. Fan, E. Parra, K. Y. Kim, I. Alexeev, and H. M. Milchberg
Institute for Physical Science and Technology, University of Maryland, College Park, Maryland 20742

J. Cooley and T. M. Antonsen
Institute for Research in Electronics and Applied Physics, University of Maryland, College Park, Maryland 20742

(Received 26 December 2001; published 3 May 2002)

We present a comprehensive report based on recent work [Phys. Rev. Lett. **84**, 3085 (2000)] on resonant self-trapping and enhanced absorption of high power Bessel beams in underdense plasmas. The trapping resonance is strongly dependent on initial gas pressure, Bessel-beam geometry, and laser wavelength. Analytic estimates, and simulations using a one-dimensional Bessel-beam-plasma interaction code consistently explain the experimental observations. These results are for longer, moderate intensity pulses where the self-trapping channel is induced by laser-heated plasma thermal pressure. To explore the extension of this effect to ultrashort, intense pulsed Bessel beams, we perform propagation simulations using the code WAKE [Phys. Rev. E **53**, R2068 (1996)]. We find that self-trapping can occur as a result of a plasma refractive index channel induced by the combined effects of relativistic motion of electrons and their ponderomotive expulsion.

DOI: 10.1103/PhysRevE.65.056408 PACS number(s): 52.38.Hb, 52.35.Mw

I. INTRODUCTION

The self-focusing process, in which a laser beam self-traps and propagates at high intensity over distances longer than its natural diffraction length scale, has been studied since the 1960s [1,2], where it was originally observed in solid or liquid transparent materials below megawatt (MW)-level laser powers. At power levels below ~10 MW, nonlinear self-focusing in neutral gases was observed [3] and in subcritical density plasmas, ponderomotive filamentation was observed at greater than gigawatt power levels [4]. Most recently, subpicosecond, terawatt (10^{12} W)-level laser pulses have been demonstrated to self-trap in plasmas as a result of nonlinear, relativistic modifications to the plasma index of refraction and ponderomotive expulsion of plasma electrons from the beam [5]. For a fixed density of the medium, all of these processes have a threshold power requiring the nonlinear lensing of the beam to overcome diffraction. Beyond the threshold power, the self-trapping effect is maintained or further enhanced.

In this paper, we present comprehensive results from recent work [6] demonstrating a new type of self-trapping. This effect occurs in the propagation of high intensity Bessel beams in underdense plasmas. However, unlike the above examples of laser beam self-trapping, the self-trapping of Bessel beams is *resonant* in nature, and this resonance is multidimensional. That is, for the relevant parameters of initial neutral gas or plasma density, laser power, laser wavelength, and Bessel-beam geometry, self-trapping will occur only over a narrow range of each of these parameters if the remainder are held fixed.

Historically, resonant laser-plasma coupling has been observed in two main instances, both for electron densities near the critical density. The first is the well-known process of resonance absorption. Here, a *P*-polarized light pulse is obliquely incident on a plasma density gradient, usually from a solid target, and it experiences increased absorption resulting from the electric field tunneling into the critical-surface region [7]. Resonance absorption was first observed in high power nanosecond laser-target experiments [8] and later studied using femtosecond pulses, where the plasma density gradient scale length could be better controlled [9]. Calculations of short pulse laser absorption by cluster plasmas have suggested that an absorption maximum exists when the solid density clusters expand to satisfy $N_e \sim 3N_{\mathrm{cr}}$, a condition determined by the resonance in the dielectric response of a plasma sphere [10]. More recent modeling of the laser-cluster interaction suggests that for most experimental situations, this resonance may actually occur near N_{cr} rather than at $3N_{\mathrm{cr}}$ [11]. In all of these prior cases of resonant laser-plasma coupling, however, the resonance is a result of the laser frequency and electron density dependence of the plasma bulk dielectric response, and no transverse spatial modification of the laser beam needs to occur (but it may occur in practice, for example, as a result of a rippled critical density surface). For Bessel beams, the self-trapping resonance not only depends on the dielectric response, but it also depends strongly on the plasma geometry, and strong transverse beam modification necessarily occurs.

To begin, we define a *generalized* Bessel beam, in a medium invariant along the optical axis z, to be a solution $E(\vec{r}_\perp, z, \omega) = e^{i\beta z} u(\vec{r}_\perp, \omega)$ of the Fourier transformed wave equation

$$\nabla_\perp{}^2 u + \kappa^2(\vec{r}_\perp, \omega) u = 0, \tag{1}$$

where

$$\kappa^2(\vec{r}_\perp, \omega) = k^2 n^2(\vec{r}_\perp, \omega) - \beta^2 = k^2[1 + \delta_{\mathrm{plasma}}(\vec{r}_\perp, \omega) + 4\pi\chi(\vec{r}_\perp, \omega)] - \beta^2 \tag{2}$$

is the square of the local transverse wave number, which allows for possible transverse variation in the refractive index n of the medium, where χ is the total atomic and ionic susceptibility and δ_{plasma} is the plasma contribution to the medium response. In the above equations, $\nabla_\perp{}^2$ is the Laplac-

ian in the transverse coordinate $\vec{r}_\perp$, $k=\omega/c$ is the vacuum wave number of the laser, and β is the wave number along the propagation axis z. For a uniform, nonabsorbing medium, the transverse wave number $\kappa=\kappa_0$ is a real constant, and Eq. (1) yields the standard Bessel-beam solution $E(r,\phi,z,\omega)=E_i e^{i\beta z}J_m(\kappa_0 r)e^{im\phi}$, where E_i is the peak electric field, and m is a positive integer. Such solutions for a uniform medium have been considered in earlier work investigating the linear [12,13] and nonlinear [14] optics of Bessel beams.

Zero-order ($m=0$) Bessel beams have been produced using phase masks, circular slits followed by lenses [12,14] or axicon lenses [6,15]. More recently, $m>0$ beams have been produced using a phase mask closely followed by an axicon [16,17]. All of these elements convert an input plane wave into a cone of rays (conical beam) converging onto the optical axis, all at the same angle γ with respect to the axis. The result of the mutual interference of these rays is the Bessel beam, with axial wave number $\beta=k\cos\gamma$. For moderate pulse energies and pulse widths, the peak intensity of a $m=0$ Bessel beam can be sufficient for breakdown of neutral gases and generation of highly elongated plasma channels. Such channels have been used for optical guiding [18], and have applications to laser-driven plasma accelerators [19], short wavelength generation [20], and high current, high speed switching [15]. Recently, a long tubular plasma has been generated through the use of fifth order Bessel beam [17], and the self-trapping of Bessel beams has been found to seed a parametric instability that results in axially periodic plasma channel modulations [21].

That resonant self-trapping should occur for intense Bessel beams was strongly suggested by earlier work of our group. In that experiment [22], low energy ($\sim$1 mJ), 1-ps white light continuum Bessel-beam probe pulses were focused onto underdense ($<10^{-2}N_{\rm cr}$) preformed plasma channels produced by a 100-ps heater (pump) Bessel-beam pulses in low pressure gases ($<$150 torr). Once a local electron density minimum appeared on the axis as a result of the plasma's radial expansion (after a few hundred picoseconds), trapping and quasiguiding of the probe pulse occurred only for certain wavelengths, for fixed pump pulse energy, initial neutral gas density, and pump-probe delay [22]. This suggested that at higher initial gas densities, the increased laser-plasma heating and more rapid formation of a suitable channel structure could result in self-trapping of the 1064-nm pump pulse during its 100-ps envelope.

The full modeling of the Bessel-beam-plasma interaction would require considering the time-dependent electromagnetic wave equation coupled to equations for the time-dependent plasma hydrodynamics. However, for our experimental situation involving 100-ps heating pulses and plasma channels of maximum diameter $\sim$100 μm [23], a quasistationary calculation is appropriate, in which time-independent equation (1) is coupled to a model of the time-dependent plasma hydrodynamics. We note that the transit time for light across a plasma channel of maximum diameter $\sim$100 μm is $<$1 ps, which is much shorter than the 100-ps laser pulse or the plasma hydrodynamics time scales. These time scales have been measured to be $\tau_a\sim 50$ ps for avalanche-driven electron density growth, $\tau_s=\lambda_{ii}/c_s\sim 100$ ps for shock development, and $\tau_c=w/c_s\sim 1$ ns for radial evolution of the plasma column [23], where λ_{ii} is the ion-ion collision mean free path, c_s is the local plasma sound speed, and w is the laser spot size. Therefore, in our numerical simulations of the time-dependent interaction (see Sec. III) we solve Eq. (1) for an evolving sequence of plasma profiles; our simulations are quasistationary.

For a stationary profile, the solution of Eq. (1) outside the plasma boundary ($r>r_b$) gives

$$E(\vec{r}_\perp,z,\omega)=\tfrac{1}{2}e^{i\beta z}[a_+H_m^{(1)}(\kappa_0 r)+a_-H_m^{(2)}(\kappa_0 r)]e^{im\phi}, \tag{3}$$

where $\kappa_0=\kappa(r>r_b)=(k^2-\beta^2+4\pi\omega^2\chi_0/c^2)^{1/2}$, $H_m^{(1,2)}$ are the mth-order Hankel functions of the first and second kind, $\chi_0=\chi(r>r_b)$, and the ratio a_+/a_- depends on the specific plasma structure. Well outside the waveguide for $r\gg r_b$ and $\kappa_0 r\gg 1$, the asymptotic forms of $H_m^{(1,2)}$ give

$$E(\vec{r}_\perp,z,\omega)\approx E_i e^{i\beta z}[e^{-i\kappa_0 r}+\eta e^{-i(m+1/2)\pi}e^{i\kappa_0 r}] \times e^{im\varphi}/(2\pi\kappa_0 r)^{1/2}, \tag{4}$$

a sum of conical waves incident upon and scattered by the plasma at the angle $\gamma=\tan^{-1}\kappa_0/\beta$ with respect to the plasma axis, where $\eta=a_+/a_-$ is the complex scattering coefficient of the outgoing wave. In the stationary limit, the fractional absorption of the Bessel beam is given by $1-|\eta|^2$.

Independent of considerations of externally supplied Bessel beams, Eq. (1) also governs the propagation of electromagnetic waves in the plasma structure itself. In that context, the solutions to Eq. (1) can be separated into several categories depending on the behavior of $\kappa^2(\vec{r}_\perp,\omega)$ for a given plasma channel $N_e(\vec{r}_\perp)$. *Excluded modes* have $\kappa^2<0$ for $|\vec{r}_\perp|<r_m$ and $\kappa^2>0$ for $|\vec{r}_\perp|>r_m$, where r_m is a radial location in the plasma. For *radiation modes* $\kappa^2>0$ for all $\vec{r}_\perp$. Solutions having $\kappa^2>0$ for $|\vec{r}_\perp|<r_m$ and $\kappa^2<0$ for all $|\vec{r}_\perp|>r_m$ are *bound modes. Leaky or quasibound* modes have $\kappa^2>0$ over a finite radial range near the center of the channel, $\kappa^2<0$ in a portion of the channel wall, and $\kappa^2>0$ beyond that region. The result is some confinement of the wave within the interior channel region where $\kappa^2>0$, but tunneling or leaking is allowed to freely propagating waves at $|\vec{r}_\perp|>r_b$. Truly bound modes are an idealization for real plasma channels because beyond the plasma boundary $|\vec{r}_\perp|>r_b$, $\kappa^2>0$ again. In our plasma channels, there are only excluded modes, radiation modes, and quasibound modes that are confined to varying degrees. Early in the plasma channel formation, the electron density is peaked in the center and only excluded modes or radiation modes are present, depending on the peak value of the electron density. Once a shock wave begins to form during radial expansion, the electron density on axis begins to dip and quasibound modes are allowed.

For idealized bound mode solutions to Eq. (1), no field exists outside the channel, and only discrete values of β are allowed. For example, for a parabolic plasma channel $N_e(r)=N_{e0}+N_{\rm cr}(r/a)^2$, where N_{e0} is the on-axis electron density and a is a curvature parameter, the discrete channel wave number is $\beta_{pm}=k^2-4\pi r_e N_{e0}-(4/w_{\rm ch}^2)(2p+m+1)$, where $w_{\rm ch}=a/(\pi r_e N_{\rm cr})^{1/2}$, r_e is the classical electron radius,

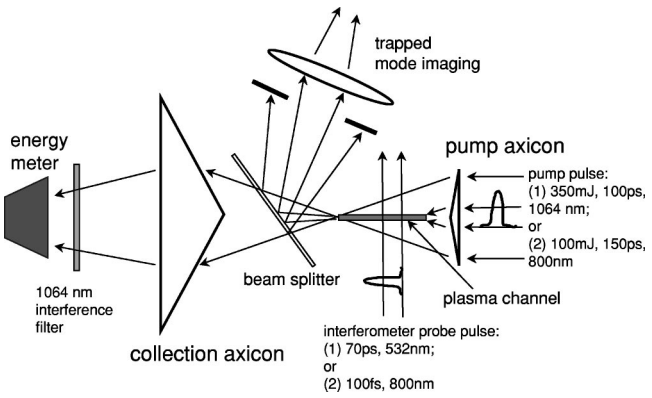

FIG. 1. Experimental setup to measure Bessel-beam trapping (from mode imaging), absorption (with collection axicon and energy meter), and plasma heating (from time resolved transverse interferometry). Pump beams were from a Nd:YAG laser system (100 ps, 1064 nm, 350 mJ) or from a Ti:Sapphire laser system (150 ps, 800 nm, 100 mJ). Axicons had base angles of 25° or 30° ($\gamma=15°$ or $\gamma=19°$). Gas fill was 20-torr N_2O with variable pressure argon. Interferometer probe pulse was 70 ps, 532 nm, 100 μJ or 70 fs, 800 nm, 1 mJ.

and p and m are radial and azimuthal mode indices [24]. For leaky mode solutions to Eq. (1), where the solutions extend beyond the plasma boundary, narrow continuous ranges of β, which we shall label β_{ch}, are favored [24]. In general, the leaky mode spectrum of solutions and their associated wave numbers β_{ch} must be calculated numerically [24]. In the region $|\overline{r_\perp}|>r_b$, these solutions can be represented as a sum given by Eq. (3), or in the limit $|\overline{r_\perp}|\gg r_b$, by Eq. (4), where β in those expressions is replaced by β_{ch}. The connection between an externally imposed Bessel beam and the electromagnetic modes of a plasma channel is then clear: resonant interaction occurs when the $\beta=k\cos\gamma$ imposed by the Bessel beam is matched to a leaky mode β_{ch} of the evolving plasma channel.

II. EXPERIMENTAL SETUP: SIMULATION CODE

Figure 1 shows the experimental setup. Pump pulses either from a Nd:YAG laser system (100 ps, 1064 nm, 350 mJ) or from a Ti:Sapphire laser system (150 ps, 800 nm, 100 mJ) were focused by axicons with base angles of 25° or 30° (which produce J_0 beams with ray approach angles of $\gamma=15°$ or $\gamma=19°$ with respect to the optical axis, where $\beta=k\cos\gamma$), making ~1–1.5 cm long plasma columns in an ambient gas of 20-torr N_2O plus a variable pressure of argon. The N_2O component, which field ionizes at $\sim 10^{13}$ W/cm^2, provides seed electrons for the uniform avalanche breakdown of Ar [23]. The relative self-trapping of the Bessel beam by its self-generated plasma was measured by integrating charge-coupled device camera (CCD) images of the mode intensity profile at the exit plane of the plasma channel.

In the event of self-trapping, the pump laser pulse is quasiconfined in the plasma channel, implying greater field amplitude there, and this was expected to result in both enhanced absorption and greater heating. For the measurement of plasma absorption (done only for the 1064-nm pump pulse), all untrapped axicon rays passing through the plasma (which form a ring), as well as the portion of the beam trapped along the plasma axis, were collected and focused by a large diameter collection axicon through a 1064-nm interference filter onto an energy meter. The additional heating generated by the enhanced absorption was measured by monitoring the channel's hydrodynamic evolution through interferometry, using variably delayed probe pulses. To capture channel evolution with picosecond resolution, a small portion of the main Nd:YAG pulse was frequency doubled (to 532 nm, 70 ps, ~100 μJ), passed through an optical delay line (−1 to 14 ns), and then directed transversely through the plasma [23], which was imaged by a two-lens system through a folded (or split) wave front interferometer. The beam is split, with the portions transversely offset, so that the interference pattern is obtained by overlapping the phase-perturbed area (resulting from the plasma) with an unperturbed area of the beam, which is used as the phase reference [25]. An uncoated ~0.25-in.-thick BK7 glass wedge split the wave front into beams reflected from the front and back surfaces, with the transverse offset determined by the wedge thickness.

For the interferometer with femtosecond resolution, the probe beam (100 fs, 800 nm, ~1 mJ) was obtained from a Ti:Sapphire laser synchronized to the Nd:YAG system with ~10 ps of jitter. Details of the synchronization can be found in Ref. [26]. The jitter originates from the Nd:YAG oscillator's active mode locker. The femtosecond probe pulse was passed through a delay line and directed transversely through the plasma, which was imaged by a two-lens system through a modified Mach-Zehnder interferometer. For the 800-nm pump pulse, the delay line was optical, using a gold-coated retroreflector, and the delay ranged from −500 ps to 1 ns. In the case of 1064-nm pump pulses, the delay could be controlled electronically in steps of 1 ns, and fine adjustment was achieved using the optical delay line. As in the picosecond setup, the two beams in the modified Mach-Zehnder interferometer were transversely offset in order to allow overlap of the phase-perturbed area of the beam with the unperturbed area. For the femtosecond case, a modified Mach-Zehnder interferometer rather than the wedge was used because the time separation of the front and back surface reflections in a wedge would greatly exceed the probe pulse duration. The picosecond interferometer was useful for measuring plasma channel evolution at times of at least ~250 ps later than the early formation phase. During and immediately after the 100- or 150-ps pump pulse, rapid ionization and shock formation occur and the 70-ps time resolution was insufficient. The femtosecond interferometer was used to examine channel evolution during the pump pulse. For the 1064-nm pump pulse, the temporal resolution was limited to ~10 ps by the Nd:YAG mode-locker jitter. For the 800-nm pump pulse, the probe was exactly synchronized, so that the resolution was limited by the transit time of the probe across the plasma (~100 fs for a 30-μm-diameter plasma column). The electron density was extracted from the interferograms by first using Fourier techniques [27] to de-

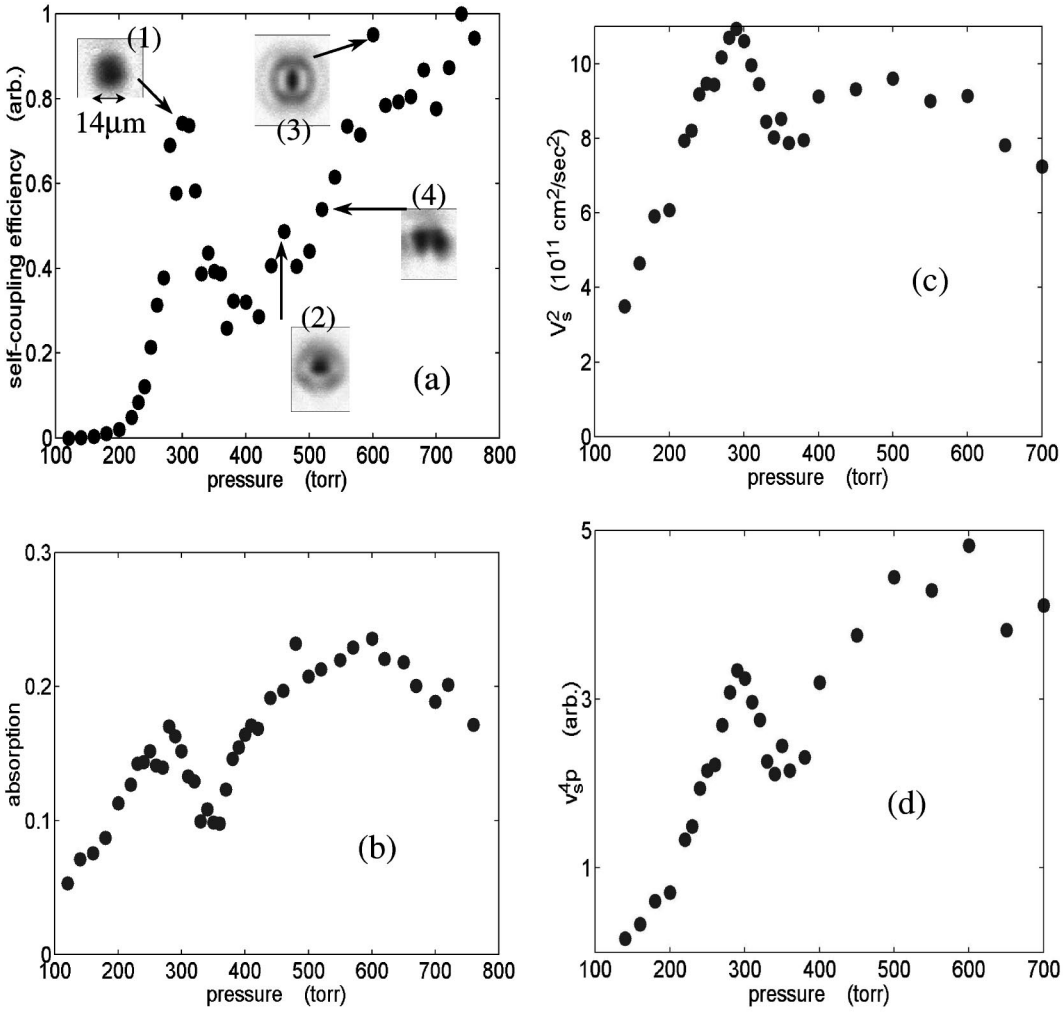

FIG. 2. (a) Relative self-trapped energy measured at channel exit versus pressure; each point is a 10 shot average. Insets are resonant mode images at different pressures. (b) Absorption efficiency versus pressure. Each point is 500 shot average. (c) Square of shock wave speed (v_s) versus pressure (P). (d) $v_s{}^4 P(\propto \varepsilon)$ versus P.

termine the phase, which was then processed using Abel inversion.

Refracted by the axicon, the pump pulse approaches the optical axis and self-interferes to form a zero-order Bessel beam with peak on-axis vacuum intensity $\sim 5 \times 10^{13}$ W/cm^2 (for the 1064-nm pump) and 2×10^{13} W/cm^2 (for the 800-nm pump). Low intensity imaging of the focus along its length with 60X magnification showed that it was axially uniform and cylindrically symmetric. At high intensities, the resulting $\sim$1–1.5 cm long plasma column produced in ambient gas was cylindrically symmetric and uniform along optical axis, except for some taper within $\sim$1 mm near the ends [23].

The self-consistent Bessel-beam plasma interaction was simulated using a quasistationary model, in which Eq. (1) is coupled to a 1D radial Lagrangian hydrocode. Starting with neutral gas, Eq. (1) is solved at each time step, yielding the complex scattering coefficient $\eta(t)$ [see Eq. (4)] as a function of time. The updated electric field then heats and ionizes the gas/plasma. A Drude model is used for the plasma dielectric response, where $\delta_{\text{plasma}}(r,\omega) = -\xi + i\xi\nu/\omega$, $\xi = (1 + \nu^2/\omega^2)^{-1} N_e(r)/N_{\text{cr}}$ and $\nu = \nu(r)$ is the collision frequency, which accounts for electron-ion and electron-neutral collisions. The model includes field ionization [28], collisional ionization, thermal conduction (both gradient-based and flux-limited), and a collisional-radiative ionization model. Because the model assumes cylindrical symmetry, the coupling to $m > 0$ electromagnetic modes is not treated.

III. EXPERIMENTAL RESULTS, CALCULATIONS, AND DISCUSSION

Several experiments were performed in order to measure the effect of varying the Bessel-beam parameters on self-trapping. The laser wavelength was varied ($\lambda = 800$ nm and 1064 nm), as was the Bessel-beam ray approach angle ($\gamma = 15°$ and 19°). Simulations were performed for these experiments.

A. 1064-nm, 100-ps pump pulse and 25° base angle axicon ($\gamma = 15°$)

Data from experiments with the 25° base angle axicon ($\gamma = 15°$) and the 5×10^{13} W/cm^2 peak intensity, 1064-nm,

100-ps pump pulse are shown in Figs. 2 and 3. The self-trapping of the Bessel beam versus gas fill pressure is plotted in Fig. 2(a). The points are 10 shot averages of the integral of the imaged channel exit mode. As the pressure increases, strongly increased coupling occurs to the $p=0$, $m=0$ lowest order mode (p is the radial mode index) with maximum coupling at ~300 torr. The mode at that pressure is shown in inset (1). At slightly higher pressures the coupling drops sharply, pointing to a resonance at 300 torr. Beyond 400 torr, the coupling increases again, now to higher order modes, although the trapped mode pattern now fluctuates slightly from shot to shot owing to channel fluctuations. At ~460 torr, the $p=1$, $m=0$ mode shown in inset (2) dominates, or appears most frequently on a shot-to-shot basis. At ~510 torr, the $m=1$ mode dominates [shown in inset (4)], while at 580 torr, the $p=2$, $m=0$ mode is favored. At pressures in between the $m=0$ points, the most frequently observed exit modes are $m>0$ modes that are closely spaced in pressure. We note that even though the generated channel is nearly cylindrically symmetric [23], slight azimuthal variations in the input beam or in the plasma are sufficient for such $m>0$ coupling [22]. As the pressure increases, there is an increase in shot-to-shot fluctuations in the optimally coupled mode (that is, in p and m), which is likely due to greater sensitivities of plasma heating and channel formation to laser energy and input beam mode fluctuations.

Figure 2(b) shows absorption of the pulse as a function of pressure. Each point is a 500 shot average. Note that the nontrapped or transmitted part of the beam collected by the second axicon was a well-defined ring; no off-forward scattering was observed from the plasma other than the trapped light, if present. The pressure dependence of the absorption corresponds well to the main coupling resonance of Fig. 2, with a clear peak at ~300 torr for the $p=0$, $m=0$ resonance. Less well-defined peaks at ~500 torr and ~600 torr likely correspond to the $p=1$, $m=0$ and the $p=2$, $m=0$ resonances, respectively, as shown in Fig. 2(a).

Direct evidence of the enhanced plasma heating from these coupling resonances is obtained from measuring the channel shock expansion velocity. As the expansion is adiabatic after the first few hundred picoseconds [23], the square of the channel expansion velocity at later times is a relative measure of the heating by the laser pulse. The channel radius R_s, taken as the position of peak electron density in the expanding shock, was measured as a function of time using the picosecond interferometer and the velocity was obtained as the time derivative of the best fit curves for the radius, which follow the dynamics of cylindrical blast waves [23,29] with excellent accuracy,

$$R_s \sim (\varepsilon/\rho_0)^{1/4} t^{1/2}, \tag{5}$$

where ε is the energy per unit length initially available to drive the expansion and ρ_0 is the initial mass density. Figure 2(c) is a plot of $v_s{}^2=(dR_s/dt)^2$ versus pressure at $t=1.6$ ns after the pump, and the peak at ~300 torr is coincident with the peaks in both the relative trapping and the absorption, which is direct evidence for enhanced heating at the trapping resonance. At ~500 torr and ~600 torr there are much less well-defined peaks that agree with the peaks corresponding to modes (2) and (3) in Figs. 2(a) and 2(b). Figure 2(d) is a plot of $v_s{}^4 P$ versus pressure (P), where $v_s{}^4 P$ is proportional to ε from Eq. (5), and ε is proportional to the absorbed energy. The similarity in the curve shapes in Figs. 2(b) and 2(d) confirms the connection between the enhanced absorption and plasma heating, and clearly illustrates the impact of the coupling resonances on the plasma hydrodynamics.

Figure 3(a) shows a simulation for total absorption

$$A=\int_{-\infty}^{\infty}(1-|\eta(t)|^2)E_i{}^2(t)dt\left[\int_{-\infty}^{\infty}E_i{}^2(t)dt\right]^{-1} \tag{6}$$

as a function of pressure for the conditions of Fig. 2: peak vacuum intensity of 5×10^{13} W/cm^2, $\lambda=1064$ nm, 100-ps pulse width, and $\gamma=15°$. The first absorption resonance is for coupling to the $p=0$, $m=0$ mode and occurs at ~300 torr, and the next $m=0$ resonances, which are far less prominent, occur at ~460 torr ($p=1$) and ~580 torr ($p=2$), all in good agreement with the peaks in Fig. 2. Coupling to $m>0$ resonances is not handled by the simulation.

The time-dependent transmission (or scattering) $|\eta(t)|^2$ of the plasma channel is shown in Fig. 3(b) for initial gas pressures of 250, 300, and 350 torr. Optimal coupling is seen to take place at 300 torr, where the strong dips in $|\eta(t)|^2$ result from dynamic resonant coupling during the pump pulse. The dips correspond to times when the input beam parallel wave number (from the axicon) closely matches the wave number of a quasibound mode of the evolving plasma channel, or $\beta=k\cos\gamma\approx\beta_{\rm ch}$. At those points, coupling to the $p=0$ $m=0$ quasibound mode is strong. At the first dip, the mode's spot radius extends beyond the shallow channel wall, outside of which the field is oscillatory (15% of peak amplitude). Figure 3(c) shows a time sequence of electric field profiles at the first dip. By 122 ps, the quasibound mode is growing until it peaks at 134 ps, where the dip is at its minimum. At the second dip near 160 ps, as shown in Fig. 3(d), the mode is more tightly bound with little field (~1% of peak amplitude) escaping outside the channel wall. In between the dips, and on either side of them, field is excluded from the channel center because $k\cos\gamma\neq\beta_{\rm ch}$. At no point during the channel evolution for the 250-torr and 350-torr cases is the resonance condition $k\cos\gamma\approx\beta_{\rm ch}$ satisfied, so strong dips in $|\eta(t)|^2$ do not appear for those fill pressures.

The effects of the coupling resonances on the plasma hydrodynamics at 300 torr are shown in Fig. 3(e), where the electron temperature at channel center $T_e(t)$, the relative incident power $P_{inc}(t)=E_i{}^2(t)$, and the absorbed power $P_{abs}(t)=(1-\eta(t)|^2)\ E_i{}^2(t)$ are plotted. As expected from the enhanced field amplitude at resonance, as shown in Figs. 3(c) and 3(d), there are spikes in the absorption and heating. The pump laser envelope is overlaid on the plot, and it is seen that the resonances occur past the midpoint of the pulse, when a channel confining structure has formed.

The existence of a self-trapping resonance at ~300 torr implies that a leaky channel develops during the pump pulse. At nearby nonresonant pressures, however, this should not occur. Using the femtosecond interferometer, we verified that

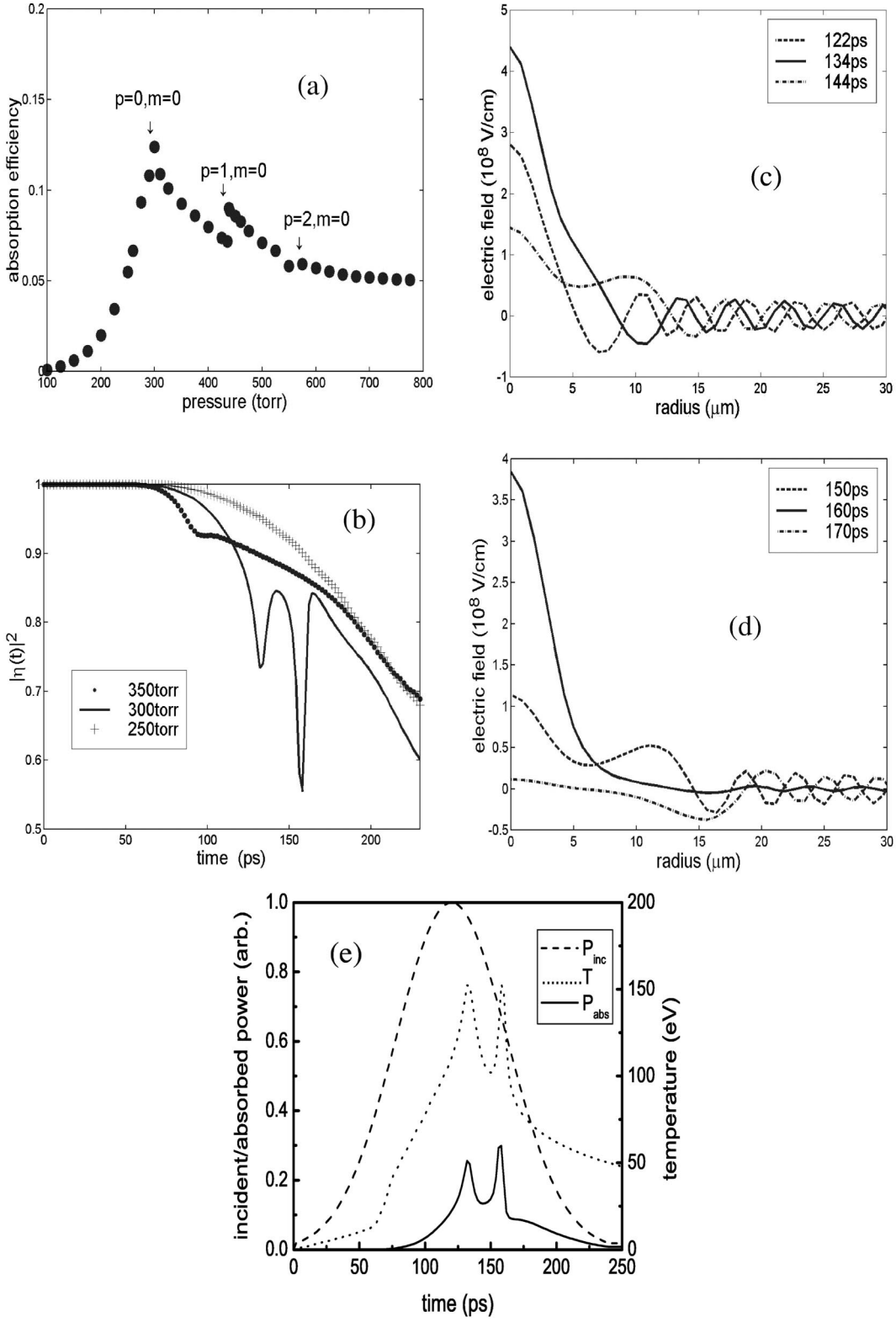

FIG. 3. (a) Calculation of absorption efficiency versus pressure. Parameters used in the calculation are the same as in the experimental results of Fig. 2. The three peaks in the absorption curve correspond to coupling to the $p=0$, $m=0$; $p=1$, $m=0$; and $p=2$, $m=0$ modes. Peak vacuum intensity of 5×10^{13} W/cm^2, $\gamma=15°$, 1064 nm, 100 ps. The pulse peak occurs at ~120 ps. (b) Calculation of time-dependent channel transmission $|\eta(t)|^2$ during the pump pulse for initial pressures 250, 300, and 350 torr. Resonant coupling occurs at 300 torr. (c) Time sequence of electric field profiles at the first dip for 300-torr curve in Fig. 3(b). (d) Time sequence of field profiles at the second dip for 300-torr curve in Fig. 3(b). (e) Relative incident and absorbed power ($P_{\rm inc}$ and $P_{\rm abs}$), and channel-center electron temperature (T_e) versus time for 300 torr.

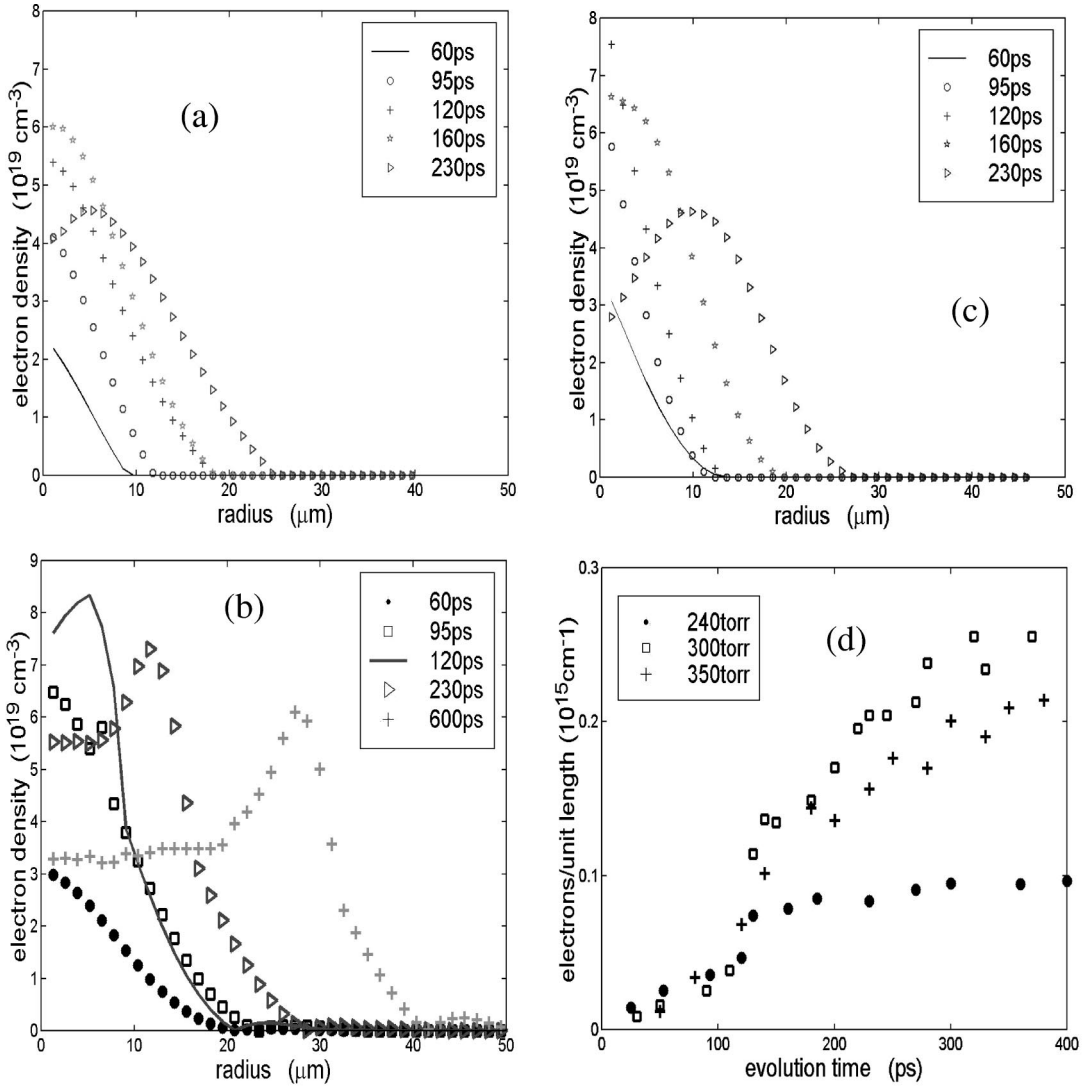

FIG. 4. (a) Time sequence of electron density profiles, for ambient gas pressure of 240 torr. (b) Time sequence of electron density profiles, for ambient gas pressure of 300 torr. (c) Time sequence of electron density profiles, for ambient gas pressure of 350 torr. (d) Number of electrons per unit length of channel versus time, for pressures 240, 300, and 350 torr.

this was the case. In Figs. 4(a), 4(b), and 4(c), electron density profiles of the plasma column are plotted in time sequence for 240 torr, 300 torr, and 350 torr gas fill pressures. The time $t=0$ is assigned to the onset of the smallest resolvable fringe perturbation in the interferograms at an electron density of $\sim 5\times 10^{17}$ cm^{-3}; the pump pulse peak occurs at $t\sim 100$ ps. For the nonresonant pressures of 240 and 350 torr, a guiding channel appears only very late in the pump pulse. During the main part of the pump pulse, the peaked on-axis electron density profile would have tended to exclude beam power from the axis. For 300 torr, as shown in Fig. 4(b), a channel forms as early as $\sim$120 ps, which is nearly the center of the pump pulse, and the channel subsequently becomes deeper and wider than at similar times in the nonresonant cases.

The stronger coupling and plasma heating at the resonant pressure can be further examined by determining the relative amounts of ionization induced by the pump pulse. A measure of the ionization is $Q(t)=\int_0^{R_{\max}} N_e(r,t) 2\pi r dr$, the number of electrons per unit length of the plasma channel, where $R_{\max}$ is the radial extent of the plasma, and $N_e(r,t)$ is electron density extracted by the femtosecond interferometer. Figure 4(d) shows Q plotted versus time for the three pressures of Figs. 4(a–c). Up until $\sim$120 ps, there is similar growth in ionization for the three pressures. Just past $\sim$120 ps, however, the ionization for 300 torr rises rapidly over a 10–20 ps interval, to a level higher than that for the other pressures. This interval is likely where resonant coupling occurs, and this possibility is consistent with the simulations of Fig. 3, where it is seen that the dips in $|\eta(t)|^2$ are 10–20 ps wide. The slow rise in Q at times longer than $\sim$200 ps results from collisional ionization at the periphery of the expanding plasma at times after the pump pulse [23,30]. Since the collisional ionization rate scales as the square of the density, the highest Q might have been expected for 350 torr, especially given the exponential growth of avalanche breakdown. Even maintaining the same ionization rate would still have resulted in higher values of Q at the higher density. However,

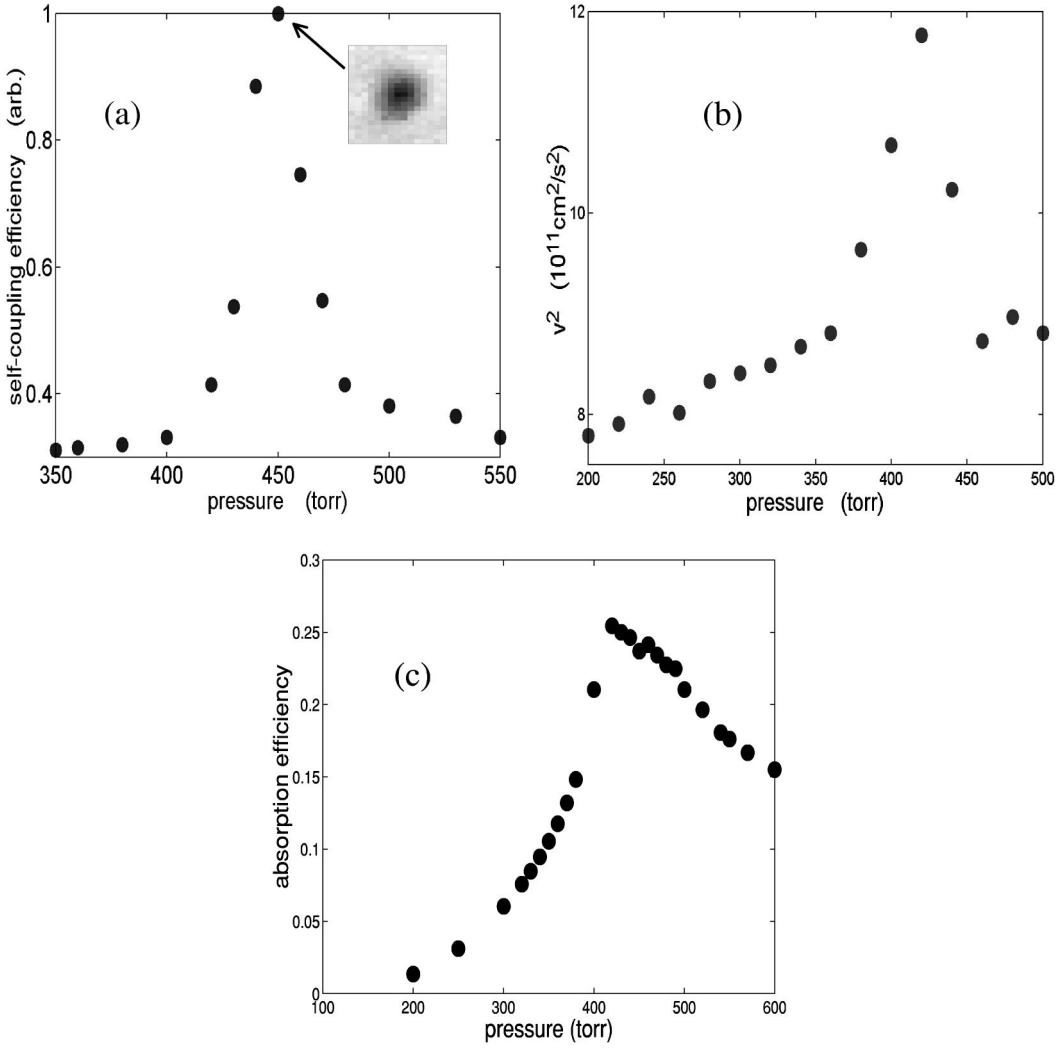

FIG. 5. Experiment and simulation results for 30° base angle axicon ($\gamma = 19°$), other parameters are the same as in Figs. 2 and 3. (a) Relative self-trapped mode energy versus pressure. Each point is a 10 shot average. The inset is the observed $p=0$, $m=0$ mode. (b) Square of shock wave speed versus pressure, obtained from interferometry. (c) Calculation of absorption efficiency versus pressure.

the striking result is that the resonance at 300 torr causes sufficiently enhanced heating to yield the maximum ionization in spite of the expected advantages of higher density.

B. 1064-nm, 100-ps pump pulse and 30° base angle axicon ($\gamma = 19°$)

A 30° base angle axicon, with a ray approach angle of $\gamma = 19°$, was substituted for the 25° axicon. All other parameters were the same as above. Figure 5(a) shows the relative self-trapping strongly peak at ~450 torr, with the lowest order $m=0$, $p=0$ self-trapped mode shown in the inset. The enhanced heating at the resonance is, as before, determined by monitoring the channel expansion velocity; Fig. 5(b) shows that the peak heating occurs at ~420 torr, in reasonable accord with the self-trapping resonance. Comparison with Fig. 2 shows that the resonant pressure is strongly dependent on the angle γ of the Bessel-beam rays approaching the optical axis. The origin of this dependence is discussed in Sec. III D. These experimental conditions were simulated using $\gamma = 19°$, with the result for total absorption as a function of pressure as shown in Fig. 5(c). The peak occurs at ~420 torr, in good agreement with the coupling and heating measurements of Figs. 5(a) and 5(b).

C. 800-nm, 150-ps pump pulse and 30° base angle axicon ($\gamma = 19°$)

Here, a 100-mJ, 150-ps pump pulse was obtained from splitting off a portion of the Ti:Sapphire beam before compression. The peak on-axis laser intensity in the axicon focus was $\sim 2 \times 10^{13}$ W/cm^2. Figure 6(a) shows relative self-trapping efficiency versus pressure, with a broad peak near ~740 torr. The inset shows the $m=0$, $p=0$ self-trapped mode at this pressure. Figure 6(b) shows the effect of the resonance on the heating: the square of the channel expansion velocity also peaks at ~740 torr. Comparison with Figs. 2 and 5 shows that the resonant pressure is strongly dependent on the wavelength of the Bessel beam. The origin of this dependence is discussed in Sec. III D. A simulation was per-

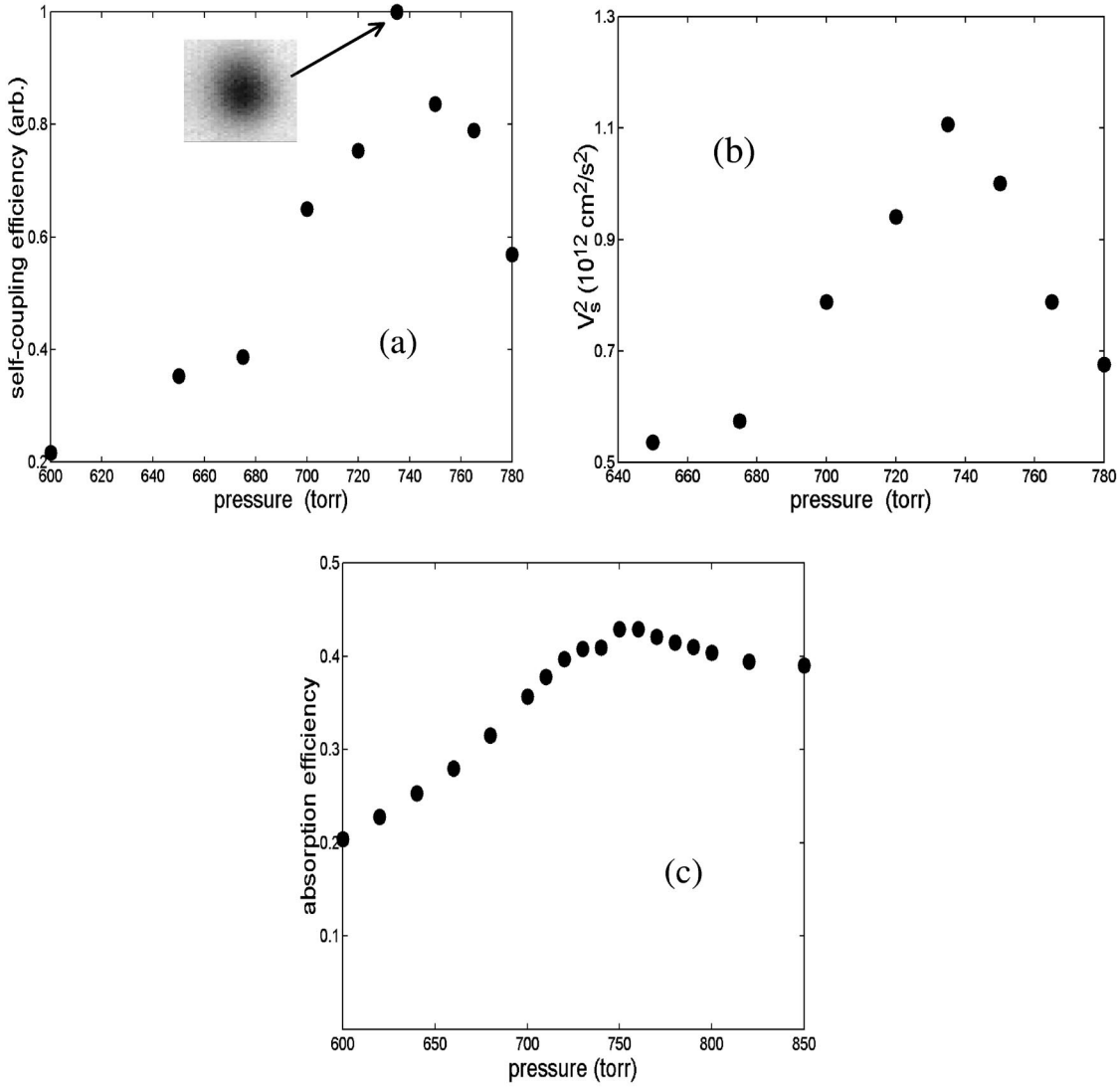

FIG. 6. Experiment and simulation results for 30° base angle axicon ($\gamma = 19°$) and pump pulse parameters: 800 nm, 150 ps, peak intensity 2×10^{13} W/cm^2. (a) Relative self-trapped mode energy versus pressure. (b) Square of shock wave speed versus pressure. (c) Calculation of absorption efficiency versus pressure.

formed using a peak intensity of $\sim 2\times10^{13}$ W/cm^2, pump pulse width of 150 ps, $\lambda = 800$ nm, and $\gamma = 19°$, with the result for pressure-dependent absorption shown in Fig. 6(c). A very broad peak around ~750 torr is seen, in good agreement with the experiments.

D. Analytic estimate of parameter sensitivity

A necessary requirement for resonant self-trapping is that $\kappa^2(r_s) < 0$, ensuring some exponential damping in the channel wall, where r_s is the radial position of the peak electron density at the shock. This is equivalent to $N_{es} > N_{\rm cr}\sin^2\gamma = N_{\rm cr}^{\rm eff}$, where $N_{es} = N_e(r_s)$. However, if $\kappa^2(r_s) < 0$, but $k\cos\gamma \neq \beta_{\rm ch}$, self-trapping will not occur and much of the wave will be reflected from the outside of the channel, where the main heating will then take place. In Fig. 3(b), the regions of the 300-torr $|\eta(t)|^2$ curve outside the dips correspond to this situation.

In any case, for given Bessel-beam parameters, the criterion $\kappa^2(r_s) < 0$ can be used to make a reasonable guess for the minimum neutral density required for self-trapping to the lowest order quasibound mode. This gives $N_{\rm min} \approx N_{\rm cr}\sin^2\gamma/Z$, where Z is the average ionization level. Using $\lambda = 1064$ nm ($N_{\rm cr} \sim 10^{21}$ cm^{-3}), $\gamma = 15°$, and argon average ionization of $Z \sim 8$ [23], gives a minimum equivalent pressure of ~240 torr, in reasonable agreement with our measurements (Fig. 2) and simulations (Fig. 3). The $\sin^2\gamma$ scaling of $N_{\rm min}$ predicts that given a resonance for $\gamma = 15°$ and $\lambda = 1064$ nm at 300 torr, the resonance for $\gamma = 19°$ and $\lambda = 1064$ nm should occur at 475 torr. This is in reasonable agreement with the measured resonant pressure of ~420–450 torr [ranging between the self-coupled mode imaging and heating measurement shown in Figs. 5(a) and 5(b)] and the simulation result of ~420 torr. The $N_{\rm cr}(\propto\lambda^{-2})$ scaling of $N_{\rm min}$ predicts that given a resonance for $\gamma = 19°$ and 1064 nm at ~435 torr [middle of the 420–450 torr range of Figs. 5(a)

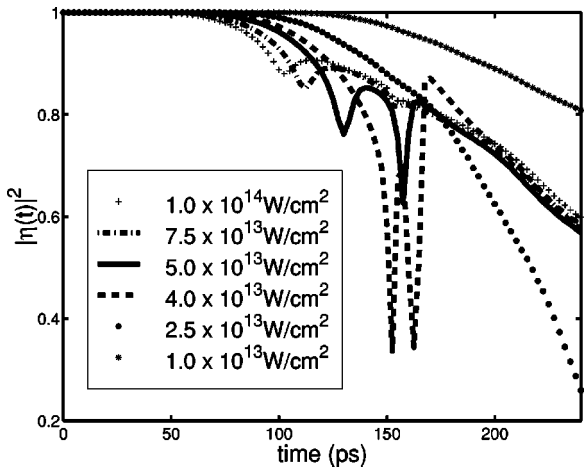

FIG. 7. Calculation of $|\eta(t)|^2$ for peak laser intensities 1×10^{13}, 2.5×10^{13}, 4×10^{13}, 5×10^{13}, 7.5×10^{13}, and 1×10^{14} W/cm^2 for the 300-torr case. Pulse parameters: 1064 nm, 100 ps, $\gamma=15°$.

and 5(b)], the resonance for $\gamma=19°$ and 800 nm should occur at ~770 torr, which is in good agreement with the measured resonant pressure of ~740 torr and the simulation result of ~750 torr.

E. Simulations of varying laser intensity

Although no experiments were performed for varying pump laser energy at fixed pulse width, simulations show that for fixed gas pressure, Bessel-beam geometry, and pulse width, self-trapping occurs over a narrow range of laser intensity. For laser wavelength of $\lambda=1064$ nm, pulse width of 100 ps, $\gamma=15°$, and Ar pressure of 300 torr, Fig. 7 shows simulation results for $|\eta(t)|^2$ for peak laser intensities of 1×10^{13}, 2.5×10^{13}, 4×10^{13}, 5×10^{13}, 7.5×10^{13}, and 1×10^{14} W/cm^2, illustrating the narrow range of the self-trapping resonance.

IV. SIMULATIONS OF THE SELF-TRAPPING OF ULTRASHORT, INTENSE BESSEL-BEAM PULSES

The previous discussion has focused on the self-trapping of pulses of sufficient duration that a plasma channel is created by hydrodynamic motion of the plasma ions during the pulse envelope. It is interesting to consider whether a similar effect can be found for ultraintense, short pulses for which the ions are essentially stationary. A channel in this case must be formed by the combined effects of relativistic motion and ponderomotive expulsion of the plasma electrons. We now present numerical simulations showing this effect for a pulse injected into a neutral gas of argon.

The simulations are carried out using the fluid version of the two-dimensional, quasistatic code WAKE [31]. This code solves for the self-consistent evolution of the laser pulse in the presence of a fluid plasma created by tunneling or field ionization of a background gas. The initial conditions are constructed to correspond to a pulse of radiation that is converging on the z axis in a cone at a specified angle γ. As the pulse's phase fronts converge on the axis, the intensity increases in the regions of constructive interference, forming the Bessel beam, and free electrons are generated by ionization. The evolution of the pulse is then affected by refraction and focusing due to the nonuniform, mildly relativistic electron plasma.

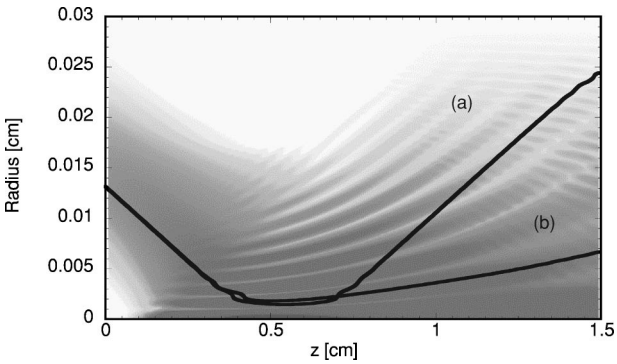

FIG. 8. Grayscale image of electron density left after passage of laser pulse. Also shown are the radii through which 25% of the pulse energy passes. Case (a) is for vacuum propagation and case (b) is for the electron density shown. The peak electron density is $N_e=N_{\max}=1.4\times10^{18}$ cm^{-3} at $r=0$ cm and $z=0.5$ cm.

Figure 8 shows a grayscale image of the electron density (as a function of r and z) created by a 1.7-J, 100-fs pulse injected at an angle $\gamma=1.72°$ ($\sin\gamma=0.03$) into 4.4 torr of argon. This small value of angle was chosen to reduce the number of radial grid points needed in the simulation. The path of the pulse as it converges on the axis is evident on the left side of the image. Also evident are striations in electron density that are the result of the nonuniform rate of ionization in the standing wave pattern (the Bessel beam) that results from the interference between the incoming and outgoing axicon rays. (Additional striations appear at the upper right corner of the image. These are artifacts associated with the reflection of rays at the simulation boundary.) The argon is ionized up to the eighth stage at the center of the line focus and this results in an electron density $N_e=N_{\max}=1.4\times10^{18}$ cm^{-3}.

The solid curves superimposed on the image in Fig. 8 give the location of the radius $R_{25\%}$ through which 25% of the laser energy passes as a function of the distance z. Two curves are shown. The curve labeled (a) shows the location of the radius $R_{25\%}$ for the case of vacuum propagation, and the curve labeled (b) shows the location of $R_{25\%}$ for the parameters under consideration. The vacuum curve shows the expected dependence of $R_{25\%}$ on z for an axicon-focused pulse. Namely, the constant energy radius decreases linearly with z, then there is a region in z of extent $\Delta z_d\approx R(1/\tan\gamma-\tan\alpha)$ [18], where the interference pattern characteristic of the Bessel beam is set up and where $R_{25\%}$ is relatively constant (where Δz_d is the Bessel-beam depth of the field or the extent of the Bessel-beam z invariance, R is the axicon input beam radius, and α is the axicon base angle), and then for larger values of z, $R_{25\%}$ increases linearly again.

The presence of plasma modifies the shape of the $R_{25\%}$ curve. The most obvious effect is that of refraction due to the generation of a large-scale electron density gradient in the radial direction. Since the refractive index of the surrounding

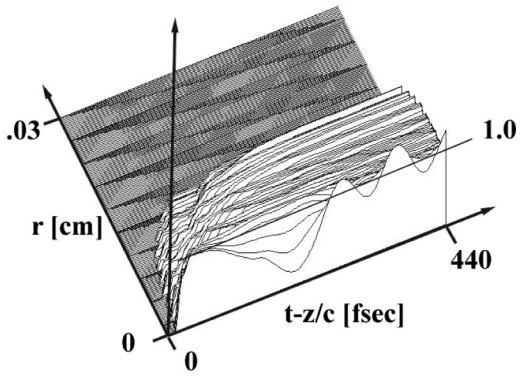

FIG. 9. The plasma contribution to the refractive index $\delta n = -\langle N_e/2\gamma_R N_{cr}\rangle$, as a function of radius and time at $z=0.67$ cm. A nonlinear potential well is created near the axis. In addition, plasma waves are excited.

neutral gas is nearly unity, the converging axicon rays are refracted parallel to the z axis at the critical angle $\theta_{cr}=\pi/2-\gamma=\sin^{-1}(1-N_e/2N_{cr})$, which gives

$$N_e/N_{cr}\approx\sin^2\gamma. \tag{7}$$

This is essentially the inverse of the refractive defocusing effect that occurs for pulses initially propagating parallel to the axis. Once refraction has succeeded in deflecting the rays, relativistic and ponderomotive effects can cause self-focusing and trapping of a portion of the pulse. Figure 9 shows the plasma contribution to the index of refraction $\delta n = -\langle N_e/2\gamma_R N_{cr}\rangle$ where the angle brackets denote an optical cycle average, N_e is the maximum electron density (effectively $8N_{argon}$, where N_{argon} is the argon neutral density) and γ_R is the relativistic factor for electrons. Generally, the index has the character needed to support quasibound modes. Namely, it is a peaked function with a small depression near the axis due to nonlinear effects. The depression contributes to self-guiding of the pulse.

The usual formula for the critical power for relativistic self-focusing in a uniform plasma, $P_{crit}=16.2\times10^9\ N_{cr}/N_e$ W [32], is a criterion derived for conventionally diffracting beams such as Gaussians. If we directly apply this to Bessel beams (which is by no means justified at this point), using our electron density criterion [Eq. (7)], we get $P_{crit}^{Bessel}=16.2\times10^9(\sin^2\gamma)^{-1}$ W. Therefore, provided sufficient electron density can be generated via field ionization, the critical power is determined entirely by the Bessel-beam geometry. For our simulation with $\gamma=1.72°$, this gives $P_{crit}^{Bessel}\sim1.8\times10^{13}$ W.

Figure 10 shows the effect on $R_{25\%}$ (at $z=1$ cm, just beyond the geometric focus of the vacuum Bessel beam, see Fig. 8) of varying the incident power around $P_{crit}^{Bessel}=1.8\times10^{13}$ W for a range of densities. For the nonzero energies shown, the minimum in $R_{25\%}$ occurs for N_e in the range $(1-2)\times10^{18}$ cm^{-3}. For $N_{cr}=1.8\times10^{21}$ cm^{-3} at 800 nm, Eq. (7) implies a γ in the range 1.4°–1.9°, roughly centered about the simulation angle of $\gamma=1.72°$. The smallest values of $R_{25\%}$ appear for powers below (0.325 J, or 0.325×10^{13} W) and near (1.77 J, or 1.77×10^{13} W) the value of

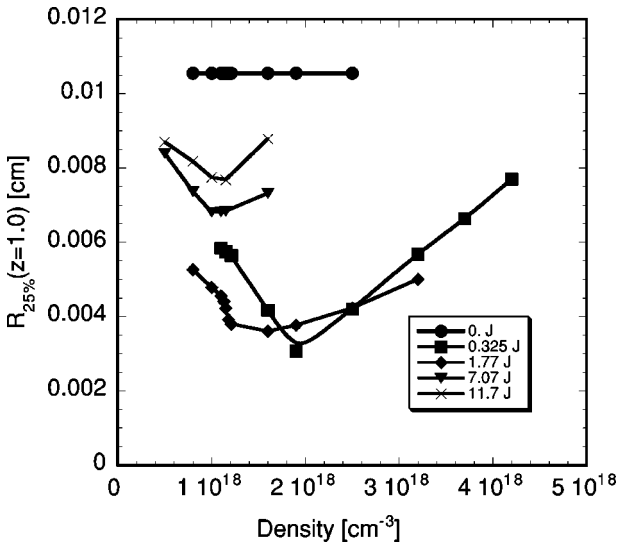

FIG. 10. $R_{25\%}$ radius versus peak electron density at $z=1.0$ cm for a range of laser pulse energies.

P_{crit}^{Bessel}. The higher power cases shown (7.07 J and 11.7 J) show substantially larger values of $R_{25\%}$.

We qualitatively explain these features as follows, although a more rigorous investigation of the critical power for Bessel-beam self-focusing will follow in future work. First, we note that the criterion $N_e/N_{cr}\sim\sin^2\gamma$ must always apply in order to effect axicon ray redirection, without which self-focusing cannot easily initiate. All the nonzero energy curves of Fig. 10 conform to this criterion. The best self-focusing would be expected to take place, however, when axicon ray redirection and relativistic index modification act in concert, and it is this situation that the expression for P_{crit}^{Bessel} attempts to describe. The curve for 0.325 J (for which $P=0.18P_{crit}^{Bessel}$), which shows the smallest $R_{25\%}$, is a possible indication that using the full beam energy in assessing P_{crit}^{Bessel} may be an overestimate. A possible reason for this is that to satisfy Eq. (7) it is sufficient that electron density must be generated only near the central lobe of the Bessel beam, not over its full radial extent. Our future work will determine what fraction of the power in the radial distribution of a Bessel beam is effectively available for self-focusing.

The larger $R_{25\%}$ for the higher power pulses may result from the generation of much wider electron density profiles from field ionization, thus inhibiting the tunneling of the Bessel beam and its trapping by the relativistic/ponderomotive index bump.

V. CONCLUSIONS

We have demonstrated electromagnetic wave self-trapping or self-focusing in plasmas that is associated with the propagation of intense Bessel beams. Unlike earlier examples of self-focusing of laser beams, Bessel-beam self-trapping is resonant in the beam parameters and in the propagation medium density. Resonant trapping of the Bessel beams is accompanied by enhanced absorption and heating. Our modeling of the Bessel beam-plasma interaction using hydrodynamic simulations shows good agreement with ex-

periments, and provides insight into the self-trapping process. A simple scaling law gives reasonable prediction of the dependence of the resonant pressure on the Bessel-beam parameters. In the breakdown of a gas by an intense Bessel beam that has plasma channel generation as a main application, resonant beam coupling can be an integral part of the process. This can lead to more efficient generation of plasma channels for certain ranges of neutral gas density. The sensitivity of Bessel-beam self-focusing to beam energy, intensity, and geometry, as well as to gas pressure may make possible a new method for stringent benchmarking of laser-plasma hydrodynamic codes.

We note that for sufficiently high pressures or long wavelengths at fixed γ, the electron density can exceed $N_{\mathrm{cr}}^{\mathrm{eff}}$ very early in the pulse during gas breakdown. This can also happen when using shallow axicons with small γ in order to make long plasma channels. In those cases, direct laser heating at the channel center can proceed only through dynamical coupling to channel resonances. Beams with some azimuthal variation will assist in this process since the $m \neq 0$ resonances at fixed p are much more closely spaced as a function of pressure than the $m=0$ resonances for varying p. In fact, comparison of the absorption measurement of Fig. 2(b) to the calculation of Fig. 3(a) shows that were it not for the coupling to $m \geqslant 1$ resonances, the absorption would show a *decreasing* trend with pressure above ~300 torr (except at the small $p=1$, $m=0$ peak at 440 torr).

For much shorter and more intense Bessel-beam pulses than those considered experimentally here, such as from high energy mode-locked Nd:glass or Ti:Sapphire laser systems, our simulations show that ponderomotive and relativistic modifications to the plasma refractive index rather than thermally driven changes can result in Bessel-beam self-trapping. The simple density criterion for self-trapping [Eq. (7)] from the quasistatic analysis is still applicable in this dynamic case, although a rigorous criterion for $P_{\mathrm{crit}}^{\mathrm{Bessel}}$ remains to be derived in future work.

ACKNOWLEDGMENTS

This work was supported by the U.S. Department of Energy and the National Science Foundation.

[1] R. Y. Chiao, E. Garmire, and C. H. Townes, Phys. Rev. Lett. **13**, 479 (1964).
[2] P. Lallemand and N. Bloembergen, Phys. Rev. Lett. **15**, 1010 (1965).
[3] V. V. Korobkin and A. J. Alcock, Phys. Rev. Lett. **21**, 1433 (1968).
[4] P. E. Young *et al.*, Phys. Rev. Lett. **61**, 2336 (1988).
[5] A. B. Borisov *et al.*, Phys. Rev. Lett. **68**, 2309 (1992); P. Monot *et al.*, *ibid.* **74**, 2953 (1995); K. Krushelnick *et al.*, *ibid.* **78**, 4047 (1997); R. Wagner *et al.*, *ibid.* **78**, 3125 (1997); J. Fuchs *et al.*, *ibid.* **80**, 1658 (1998).
[6] J. Fan, E. Parra, and H. M. Milchberg, Phys. Rev. Lett. **84**, 3085 (2000).
[7] N. G. Denisov, Zh. Eksp. Teor. Fiz. **31**, 609 (1956) [Sov. Phys. JETP **4**, 544 (1957)]; V. L. Ginzburg, *Propagation of Electromagnetic Waves in Plasmas* (Pergamon, New York, 1970); J. P. Friedberg *et al.*, Phys. Rev. Lett. **28**, 795 (1972).
[8] K. R. Manes *et al.*, Phys. Rev. Lett. **39**, 281 (1977); A. Maaswinkel, K. Eidmann, and R. Sigel, Phys. Rev. Lett. **42**, 1625 (1979).
[9] U. Teubner *et al.*, Phys. Rev. Lett. **70**, 794 (1993).
[10] T. Ditmire, T. Donnelly, A. M. Rubenchik, R. W. Falcone, and M. D. Perry, Phys. Rev. A **53**, 3379 (1996).
[11] H. M. Milchberg, S. J. McNaught, and E. Parra, Phys. Rev. E **64**, 056402 (2001).
[12] J. Durnin *et al.*, Phys. Rev. Lett. **58**, 1499 (1987).
[13] P. Sprangle and B. Hafizi, Phys. Rev. Lett. **66**, 837 (1991); B. Hafizi, E. Esarey, and P. Sprangle, Phys. Rev. E **55**, 3539 (1997).
[14] T. Wulle and S. Herminghaus, Phys. Rev. Lett. **70**, 1401 (1993).
[15] F. V. Bunkin, V. V. Korobkin, Yu. A. Kurinyi, L. Ya. Polonsky, and L. N. Pyatnitsky, Kvant. Elektron. (Moscow) **10**, 443 (1983) [Sov. J. Quantum Electron. **13**, 254 (1983)]; L. Ya. Polonsky and L. N. Pyatnitsky, Opt. Atmos. **1**, 86 (1988).
[16] N. E. Andreev, S. S. Bychkov, V. V. Kotlyar, L. Ya Margolin, L. N. Pyatnitsky, and P. G. Serafimovich, Quantum Electron. **26**, 126 (1996).
[17] J. Fan *et al.*, Phys. Rev. E **62**, R7603 (2000).
[18] S. P. Nikitin *et al.*, Phys. Rev. E **59**, R3839 (1999); C. G. Durfee, J. Lynch, and H. M. Milchberg, Phys. Rev. E **51**, 2368 (1995).
[19] E. Esarey, P. Sprangle, and A. Ting, IEEE Trans. Plasma Sci. **24**, 252 (1996).
[20] H. M. Milchberg *et al.*, Phys. Rev. Lett. **75**, 2494 (1995); J. Opt. Soc. Am. B **12**, 731 (1995).
[21] J. Cooley, T. M. Antonsen, J. Fan, E. Parra, H. M. Milchberg, L. Ya. Margolin, and L. N. Pyatnitsky (to be published).
[22] T. R. Clark and H. M. Milchberg, Phys. Rev. Lett. **81**, 357 (1998).
[23] T. R. Clark and H. M. Milchberg, Phys. Rev. Lett. **78**, 2373 (1997).
[24] T. R. Clark and H. M. Milchberg, Phys. Rev. E **61**, 1954 (2000).
[25] J. A. Stamper, S. H. Gold, S. P. Obenschain, E. A. McLean, and L. Sica, J. Appl. Phys. **52**, 6562 (1981).
[26] S. P. Nikitin *et al.*, Opt. Lett. **22**, 1787 (1997).
[27] M. Takeda, H. Ina, and S. Kobayashi, J. Opt. Soc. Am. B **72**, 156 (1981).
[28] M. V. Ammosov, N. B. Delone, and V. P. Krainov, Sov. Phys. JETP **64** 1191 (1987) [Zh. Eksp. Teor. Fiz. **91**, 2008 (1986)].
[29] L. Sedov, *Similarity and Dimensional Methods in Mechanics* (Academic, New York, 1959).
[30] T. R. Clark and H. M. Milchberg, Phys. Rev. E **57**, 3417 (1998).
[31] P. Mora and T. M. Antonsen, Jr., Phys. Rev. E **53**, R2068 (1996); Phys. Plasmas **4**, 217 (1997).
[32] G. Schmidt and W. Horton, Comments Plasma Phys. Controlled Fusion **9**, 85 (1985).